Appl. Phys. B manuscript No.
(will be inserted by the editor)

Generation of optical frequency combs via four-wave mixing processes for low- and medium-resolution astronomy

M. Zajnulina[1], J. M. Chavez Boggio[1], M. Böhm[2], A. A. Rieznik[3], T. Fremberg[1], R. Haynes[1], M. M. Roth[1]

[1] innoFSPEC-VKS, Leibniz Institute for Astrophysics Potsdam (AIP), An der Sternwarte 16, 14482 Potsdam, Germany
[2] innoFSPEC-InFaSe, University of Potsdam, Am Mühlenberg 3, 14476 Potsdam, Germany
[3] Instituto Tecnologico de Buenos Aires and CONICET, Buenos Aires, Argentina

Received: date / Revised version: date

Abstract We investigate the generation of optical frequency combs through a cascade of four-wave mixing processes in nonlinear fibres with optimised parameters. The initial optical field consists of two continuous-wave lasers with frequency separation larger than 40 GHz (312.7 pm at 1531 nm). It propagates through three nonlinear fibres. The first fibre serves to pulse shape the initial sinusoidal-square pulse, while a strong pulse compression down to sub-100 fs takes place in the second fibre which is an amplifying erbium-doped fibre. The last stage is a low-dispersion highly nonlinear fibre where the frequency comb bandwidth is increased and the line intensity is equalised. We model this system using the generalised nonlinear Schrödinger equation and investigate it in terms of fibre lengths, fibre dispersion, laser frequency separation and input powers with the aim to minimise the frequency comb noise. With the support of the numerical results, a frequency comb is experimentally generated, first in the near infra-red and then it is frequency-doubled into the visible spectral range. Using a MUSE-type spectrograph, we evaluate the comb performance for astronomical wavelength calibration in terms of equidistancy of the comb lines and their stability.

1 Introduction

Optical frequency combs (OFCs) provide an array of phase-locked equidistant spectral lines with nearly equal intensity over a broad spectral range. Since their inception, they have triggered the development of a wide range of fields such as metrology for frequency synthesis [1], for supercontinuum generation [2,3], in the telecommunication for component testing, optical sampling, and ultra-high capacity transmission systems based on optical time-devision multiplexing [4,5,6,7,8,9], or even for mimicking the physics of an event horizon [10].

One interesting application of OFCs is the calibration of astronomical spectrographs. Currently, wavelength calibration of astronomical spectrographs uses the light of spectral emission lamps (Th/Ar, He, Ne, Hg, etc.) or absorption cells, for instance, iodine cells to map the dispersion function of the spectrograph [11]. These sources provide reliable and well characterised emission and absorption spectra, respectively, but have limitations in the spectral coverage. Moreover, because these lamps provide a line spacing and a line strengths that are irregular, the wavelength calibration accuracy is below optimal [12,13,14].

High-resolution applications like the search for extrasolar planets via the observation of the stellar radial velocities' Doppler shifts and the measurement of the cosmological fundamental constants require an accuracy of a few cm/s in terms of radial velocity [15,16,17]. The resolution of Th/Ar lamps is, however, limited to a few m/s. Due to their properties, OFCs from mode-locked lasers were proposed as an ideal calibration source since they provide a much larger number of spectral lines at regions inaccessible for current lamps and with more equalised intensity [12,18]. In has been demonstrated that broadband OFCs improved the accuracy by almost three orders of magnitude down to the cm/s−level. However, due to the tight spacing of their comb lines, mode-locked lasers have to be adapted using a set of stabilised Fabry-Perot cavities in order to increase their line spacing from hundreds of MHz to $1-25$ GHz. Frequency combs that were adapted using this technique have been successfully tested for high-resolution spectrographs ($R \geq 70000$) in the visible and near infra-red (IR) [13,14,17,18,19,20, 21,22,23,24]. However, for low- and medium-resolution applications the filtering approach would require unfeasibly high-finesse stable Farby-Perot cavities to increase the spacing from hundreds of MHz to hundreds of GHz.

Using monolithic microresonators, OFCs with a frequency line spacing between 100 GHz and 1 THz (suitable for the medium- and low-resolution range) have

been recently demonstrated [25,26]. However, due to the thermal effects, microresonator-based combs cannot sustain the resonance condition for a long time and have to be regularly adjusted.

Another approach suitable for low- and medium-resolution consists of generating a cascade of four-wave mixing (FWM) processes in optical fibres starting from two lasers. This allows OFCs to be generated with, in principle, arbitrary frequency spacing. This approach has been already extensively studied with the aim to generate ultra-short pulses at high repetition rates [4,5,6,7, 8,9,27]. But also some approaches specifically targeting the task of the OFC generation in highly nonlinear fibres were numerically and experimentally studied in the recent past [28,29,30].

We numerically investigate the four-wave mixing cascade approach with the particularity that it involves a long piece of an erbium-doped fibre with anomalous dispersion where strong pulse compression based on the higher-order soliton compression takes place [31,32,33]. We focus the analysis on how the quality of the compression and the pulse pedestal build-up depend on the input power, laser frequency separation, and group-velocity dispersion of the first fibre. We investigate how the intensity noise and the pulse coherence also depend on these parameters. Studies on the length optimisation of the first and second fibre stage allowing low-noise system performance are also carried out. Using a MUSE-type spectrograph, we experimentally demonstrate that the introduced approach is suitable for astronomical applications in the low- and medium-resolution range.

The paper is structured as follows: in Sec. 2.1, we describe the approach for the generation of OFCs in fibres and, subsequently in Sec. 2.2, the according mathematical model based on the generalised nonlinear Schrödinger equation (GNLS). We present our results on the fibre length optimisation in Sec. 3. In Sec. 4, we show the results on the figure of merit and the pedestal content. The results of the noise evolution and coherence studies are shown in Sec. 5 and Sec. 6, respectively. In Sec. 7, we present the result on the experimental realisation of the proposed approach in the near IR and the visible spectral range. Finally, we draw our conclusions in Sec. 8.

2 Optical frequency comb approach and mathematical model

2.1 Four-wave-mixing based frequency comb

Fig. 1 shows the experimental arrangement used to generate broadband optical frequency combs in the near IR spectral region. The starting optical field consists of two independent and free-running continuous-wave (CW) lasers. Both lasers have equal intensity and feature relative frequency stability of 10^{-8} over one-day time frame that is typical for state-of-the-art lasers. This stability is adequate for calibration of low- and medium-resolution astronomical spectrographs, no additional stabilising techniques like laser phase-locking are required. The first laser (LAS1) is fixed at the angular frequency ω_1, while the second laser (LAS2) has a tuneable angular frequency ω_2 so that the resulting modulated sine-wave has a central frequency $\omega_c = (\omega_1 + \omega_2)/2$.

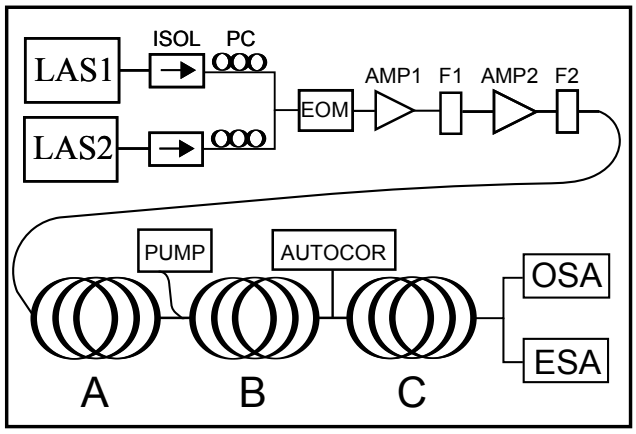

Fig. 1 Experimental setup for generation of OFCs in fibres. ISOL: optical isolator, PC: polarisation controller, EOM: electro-optical modulator, LAS1: fixed CW laser, LAS2: tunable CW laser, AMP1: Er-doped fibre amplifier 1, F1: optical bandpass filter 1, AMP2: Er-doped fibre amplifier 2, F2: optical bandpass filter 2, A: single-mode fibre, B: Er-doped fibre, C: highly nonlinear low-dispersion fibre, PUMP: pump laser for fibre B, AUTOCOR: optical autocorrelator, OSA: optical spectrum analyser, ESA: electrical spectrum analyser

The evolution of a frequency comb in this system is governed by the following processes: as the two initial laser waves at ω_1 and ω_2 propagate through the fibre A, they interact through FWM and generate a cascade of new spectral components [10,44]. The new components are phase-correlated with the original laser lines, the frequency spacing between them coincides with the initial laser frequency separation $LFS = |\omega_2 - \omega_1|/2\pi$. In the time domain, this produce a moulding of the sinusoidal-square pulse: a train of well separated higher-order solitons with pulse widths of a few pico-seconds is generated [46,47]. These higher-oder solitons undergo further compression as they propagate through the amplifying fibre B [37,48,49]: sub-100 fs pulses are generated (Fig. 2) [50]. The last stage is a low-dispersion highly nonlinear fibre where the OFC gets broadened and the intensity of the comb lines fairly equalised.

2.2 Generalised nonlinear Schrödinger equation

We model the propagation of the bichromatic optical field using the generalised nonlinear Schrödinger equation (GNLS) for a slowly varying amplitude $A = A(z,t)$

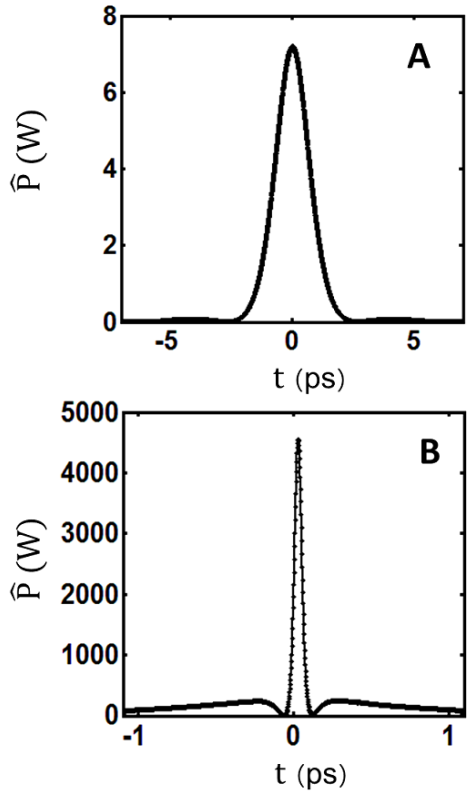

Fig. 2 Optical pulse shapes after propagation in fibre A and B obtained by means of numerical simulations for laser frequency separation $LSF = 80$ GHz and initial power $P_0 = 2$ W

in the co-moving frame [31,32,48,38,51]:

$$\frac{\partial A}{\partial z} = i\sum_{k=2}^{K}\frac{i^k}{k!}\beta_k\frac{\partial^k A}{\partial t^k} + i\gamma\left(1+\frac{i}{\omega_c}\frac{\partial}{\partial t}\right)A\mathcal{R} + g_{\mathrm{Er}}A, \quad (1)$$

where $\beta_k = \left(\frac{\partial^k \beta}{\partial \omega^k}\right)_{\omega=\omega_c}$ denotes the value of the dispersion order at the carrier angular frequency ω_c. The nonlinear parameter γ is defined as $\gamma = \frac{\omega_c n_2}{cS}$ with n_2 being the nonlinear refractive index of silica, S the effective mode area, and c speed of light. The integral $\mathcal{R} = \int_{-\infty}^{\infty} R(t')|A(z,t-t')|^2 dt'$ represents the response function of the nonlinear medium

$$R(t) = (1-f_R)\delta(t) + f_R h_R(t), \quad (2)$$

where the electronic contribution is assumed to be nearly instantaneous and the contribution set by vibration of silica molecules is expressed via $h_R(t)$. $f_R = 0.245$ denotes the fraction of the delayed Raman response to the nonlinear polarisation. As for $h_R(t)$, it is defined as follows:

$$h_R(t) = (1-f_b)h_a(t) + f_b h_b(t), \quad (3)$$

$$h_a(t) = \frac{\tau_1^2+\tau_2^2}{\tau_1\tau_2^2}\exp\left(-\frac{t}{\tau_2}\right)\sin\left(\frac{t}{\tau_1}\right), \quad (4)$$

$$h_b(t) = \left(\frac{2\tau_b - t}{\tau_b^2}\right)\exp\left(-\frac{t}{\tau_b}\right) \quad (5)$$

with $\tau_1 = 12.2$ fs and $\tau_2 = 32$ fs being the characteristic times of the Raman response and $f_b = 0.21$ representing the vibrational instability of silica with $\tau_b \approx 96$ fs [48,38, 51]. g_{Er} in the last term on the right-hand side of Eq. 1 represents the normalised frequency-dependent Er-gain. Generally, g_{Er} is a function of z. Here, we use a gain profile that does not change with z. This approach is justified by the fact that our numerical data are in a good agreement with the experimental ones. The Er-gain g_{Er} is valid only for fibre B and is set to $g_{\mathrm{Er}} = 0$ for fibres A and C.

The initial condition at $z = 0$ for Eq. 1 reads as

$$A_0(t) = \sqrt{P_0}\sin(\omega_c t) + \sqrt{n_0(t)}\exp\left(i\phi_{\mathrm{rand}}(t)\right), \quad (6)$$

where the first term describes the two-laser optical field with a peak power of P_0 and a central frequency $\omega_c = (\omega_1+\omega_2)/2$ that coincides with the central wavelength of $\lambda_c = 1531$ nm. The second term in Eq. 6 describes the noise field and has the form of a randomly distributed floor with an amplitude varying between 0 and $\sqrt{n_0}$ and a phase ϕ_{rand} randomly varying between 0 and 2π. To mimic the experimental procedure in more detail, we convolve the noise floor with two filter functions having Gaussian shapes with a width of 30 GHz and a depth of 20 dB (see Fig. 3). The maximum of each Gaussian is positioned at the respective laser frequency line as shown in Fig. 3.

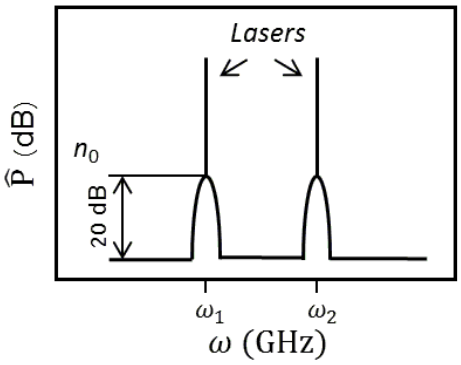

Fig. 3 Schematic representation of the initial condition

The numerical solution of Eq. 1 having the initial optical field given by Eq. 6 is performed using the interaction picture method in combination with the local error method [43,44]. Low numerical error is obtained by choosing 2^{16} sample points in a temporal window of 256 ps.

We consider up to the third order dispersion in our simulations, i.e. $K = 3$ in Eq. 1. Further, for the whole set of simulations, the following parameters for fibres A, B, and C are chosen: $\gamma^A = 2$ W^{-1}km^{-1}, $\beta_2^B = -14$ ps^2/km, $\gamma^B = 2.5$ W^{-1}km^{-1}, $\beta_2^C = 0.05$ ps^2/km, $\gamma^B = 10$ W^{-1}km^{-1}. The length of fibre C is set to $L^C = 1.27$ m. These

parameters represent material features of fibres that can be used in a real experiment.

3 Optimum lengths of fibres A and B

The aim of the propagation of the initial bichromatic field through fibres A and B is to generate maximally compressed optical pulses with a minimum level of intensity noise (IN). As the optical pulses propagate through fibres A and B, their intensity experiences periodical modulation over the propagation distance [45]. This periodicity in the peak power occurs due to the formation and the subsequent propagation of higher-order solitons [33, 41].

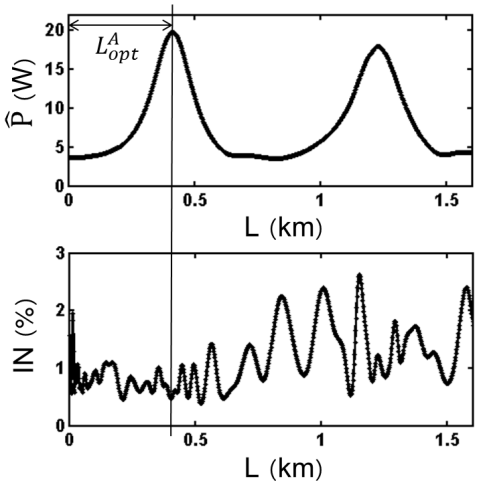

Fig. 4 Peak power in W (upper graph) and intensity noise in % (lower graph) vs. propagation distance in km for fibre A

We define the optimum length L_{opt} of a fibre as the propagation distance between the beginning of the fibre and the first pulse intensity maximum. At the same time, the optimum length denotes the propagation distance point of the maximum optical-pulse compression and, thus, of the broadest possible spectrum [36].

Rare-earth doped fibres are regarded as noisy environments and usually their lengths are kept as short as possible to avoid nonlinearities. Thus, the length optimisation studies provide us also with system parameters required to generate low intensity noise (IN) pulses and, so, low-noise OFCs. Fig. 4 and Fig. 5 show that the pulse IN has a local minimum at optimum lengths of fibre A (L^A_{opt}) and B (L^B_{opt}). A more detailed discussion of intensity noise will be done in Sec. 5.

To perform the optimisation studies, we assume the optical losses to be negligible, i.e. $\alpha = 0$ dB/km (see Eq. 1).

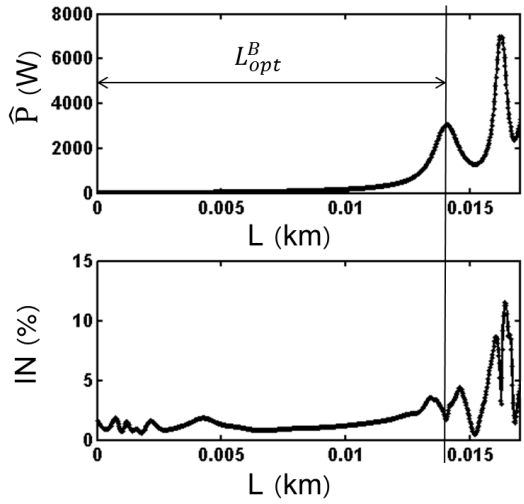

Fig. 5 Peak power in W (upper graph) and intensity noise in % (lower graph) vs. propagation distance in km for fibre B

3.1 Optimum lengths of fibre A and B depending on the initial laser frequency separation

We consider three values of the initial laser frequency separation, i.e. LFS = 40 GHz (312.7 pm), LFS = 80 GHz (625.5 pm), and LFS = 160 GHz (1.25 nm at 1531 nm) that correspond to the medium and low resolution of $R = 15000$, 7500, and 3750 at 1531 nm taking into account that an optimum spacing between the comb lines is 3-4 times the spectrograph resolution (cf. [19]). Having these values of LFS, we look for optimum lengths of fibre A and B, i.e. L^A_{opt} and L^B_{opt}, for different values of the input power P_0. For the studies, the group-velocity dispersion (GVD) parameter of fibre A is set to be $\beta_2^A = -15$ ps^2/km.

Fig. 6 illustrates the dependence of optimum lengths on the input power P_0. Generally, solitons with higher order numbers evolve on shorter lengths scales [37]. In our case, the soliton number can be calculated as

$$N^A = \sqrt{\frac{\gamma^A P_0}{(2\pi LFS)^2 |\beta_2^A|}} \tag{7}$$

for fibre A, or as

$$N^B = \sqrt{\frac{(T_0^A)^2 \hat{P} \gamma^B}{|\beta_2^B|}} \tag{8}$$

for fibre B [36], where γ^A denotes the nonlinear parameter of fibre A, $T_0^A \approx T^A_{\mathrm{FWHM}}/1.763$ is the natural width of pulses after fibre A [38], and $\hat{P}$ is the according peak power. The dependence of N on $\sqrt{P_0}$ or $\sqrt{\hat{P}}$ explains the decrease of L^A_{opt} and L^B_{opt} as the value of P_0 increases.

For the case of fibre A, the decrease of optimum-length values is preceded by a plateau region where L^A_{opt}

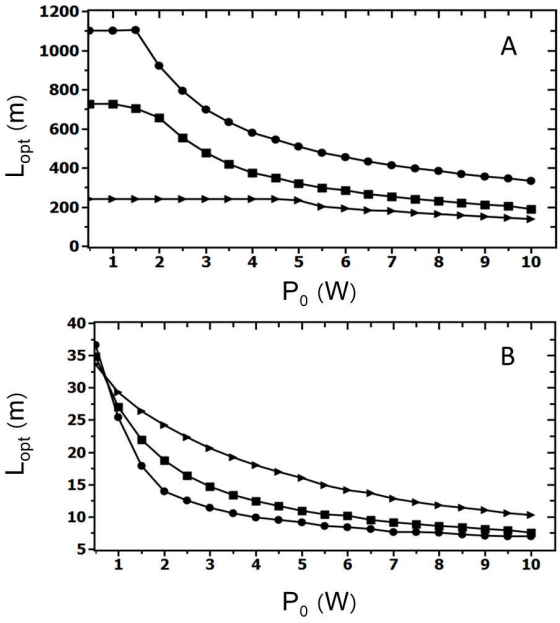

Fig. 6 Optimum lengths of fibres A and B, L^A_{opt} and L^B_{opt}, in m vs. input power P_0 in W for different values of the initial laser frequency separation LFS : $LFS = 40$ GHz (circles), $LFS = 80$ GHz (rectangles), and $LFS = 160$ GHz (triangles)

is constant as a function of P_0. In this region, P_0 is not sufficient to induce the nonlinearity that can effectively compress the initial sine wave into a train of solitons. The edge of the plateau ends denotes the the value of P_0 from which on the formation of solitons is fully supported. In terms of soliton order, $N^A < 1$ within the plateau region and $N^A \geq 1$ for higher value of P_0.

According to Eq. 7, the soliton order numbers in fibre A are inversely proportional to LFS. For instance, we have $N^A = 2.3$ for $LFS = 40$ GHz, $N^A = 1.6$ for $LFS = 80$ GHz, and $N^A = 1.15$ for $LFS = 160$ GHz at $P_0 = 5$ W. Therefore, one would expect that L^A_{opt} goes up with LFS. As Fig. 6 shows, this is not the case: L^A_{opt} is inversely proportional to LFS. We explain this phenomenon as follows: the level of complexity of the soliton's structure and the evolution behaviour grows with its order. For the initial sine-wave to be compressed into a train of solitons with higher order, it needs to propagate a longer distance so that the fibre nonlinearity can mould the pulses properly. In any case, more precise studies are needed to analyse the formation of higher-order solitons out of a sine-square wave.

However, the soliton-oder scheme works perfectly for fibre B: L^B_{opt} increases with LFS. Fig. 6 shows that the optimum lengths take the values 150 m $< L^A_{opt} \leq 1100$ m for fibre A, whereas for fibre B 7 m $< L^A_{opt} < 35$ m. Since in our case the optimum performance is shown for $LSF = 80$ GHz, we will use this value for further studies.

3.2 Optimum lengths of fibre A and B depending on the group-velocity dispersion of fibre A

The dependency of the optimum fibre length as a function of three different values of the GVD parameter of fibre A is illustrated in Fig. 7. The three dispersion values of fibre A are: $\beta^A_2 = -7.5$ ps^2/km, $\beta^A_2 = -15$ ps^2/km, and $\beta^A_2 = -30$ ps^2/km. These are standard values for single-mode fibres [2,39,40]. The initial laser frequency separation is set to be $LFS = 80$ GHz.

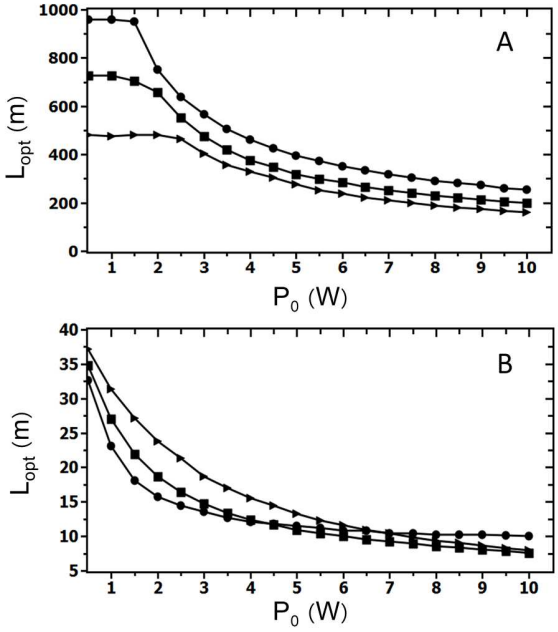

Fig. 7 Optimum lengths of fibres A and B, L^A_{opt} and L^B_{opt}, in m vs. input power P_0 in W for different values of the GVD parameter of fibre A: $\beta^A_2 = -7.5$ ps^2/km (circles), $\beta^A_2 = -15$ ps^2/km (rectangles), and $\beta^A_2 = -30$ ps^2/km (triangles)

The optimum lengths for both, fibre A and B, decrease as the value of P_0 increases. Depending on the value of P_0, the optimum length of fibre A takes the values 180 m $< L^A_{opt} <$ 980 m, for fibre B 7.5 m $< L^B_{opt} <$ 37.5 m. Also for different values of β^A_2, there plateaus of optimum length values for low input power. Precisely, the plateau region is 0.5 W $\leq P_0 <$ 1.3 W for $\beta^A_2 = -7.5$ ps^2/km, 0.5 W $\leq P_0 <$ 1.5 W for $\beta^A_2 = -15$ ps^2/km, and 0.5 W $\leq P_0 <$ 2.5 W for $\beta^A_2 = -30$ ps^2/km. In fibre A, the value of L^A_{opt} increases as the absolute value of β^A_2 decreases, whereas it is the opposite dependency in fibre B. For further studies, we use, however, the value of $\beta^A_2 = -15$ ps^2/km.

4 Figure of merit and pedestal content

The higher-order soliton compression in an amplifying medium can be considered as an alternative technique to

the compression in dispersion-decreasing fibres [34,35]. However, the compression of pico-second pulses suffers from the loss of the pulse energy into an undesired broad pedestal containing up to 70% of the total pulse energy [34,36]. This has a reduction of the pulse peak power as a result leading to the degradation of the peak-power dependent FWM process.

To describe the amount of energy that remains in the pulse and not in the pedestal, we introduce a figure of merit that is defined as:

$$FoM = \frac{\text{Pulse peak power}}{\text{Pulse average power}}. \tag{9}$$

Using the FoM, we address the following questions in this section:

- How does the FoM of fibre B changes with the initial input power?
- How does the FoM of fibre B depends on the initial LFS and β_2^A?
- How the pedestal content depends on the the initial LFS and β_2^A?

We define the pedestal content as a relative difference between the total energy of one single pulse and the energy of an approximating sech-profile with the same peak power and the FWHM as the pulse [34,36]:

$$PED = \frac{|E_{\text{total}} - E_{\text{sech}}|}{E_{\text{sech}}} \cdot 100\%. \tag{10}$$

The sech-profile was chosen, because the pulses are molded into solitons in fibre A. The energy of a soliton with a sech-profile with peak power $\hat{P}$ and a FWHM is given by

$$E_{\text{sech}} = 2\hat{P}\frac{\text{FWHM}}{1.763}. \tag{11}$$

4.1 Figure of merit and pedestal content of fibre B depending on the initial laser separation

To study the dependence of the figure of merit and the pedestal content in fibre B on the initial LFS, we set again $LFS = 40$ GHz, $LFS = 80$ GHz, $LFS = 160$ GHz and $\beta_2^A = -15$ ps^2/km.

Fig. 8 shows that the value of FoM in fibre B is generally larger for smaller values of the initial LFS. For $LSF = 40$ GHz and $LSF = 80$ GHz, FoM has a rapid increase for low input powers, reaches a maximum ($FoM = 151$ at $P_0 = 1.5$ W for $LSF = 40$ GHz and $FoM = 93$ at $P_0 = 4$ W for $LSF = 80$ GHz) and starts to decrease as the value of P_0 increases further. A similar behaviour occurs for $LFS = 160$ GHz with a maximum lying beyond $P_0 = 10$ W.

After decreasing of the pedestal content for low input powers, the value of PED reaches a minimum ($PED = 48.5\%$ at $P_0 = 3$ W for $LFS = 40$ GHz and only $PED = 30\%$ at $P_0 = 5$ W for $LFS = 80$ GHz) and then increases

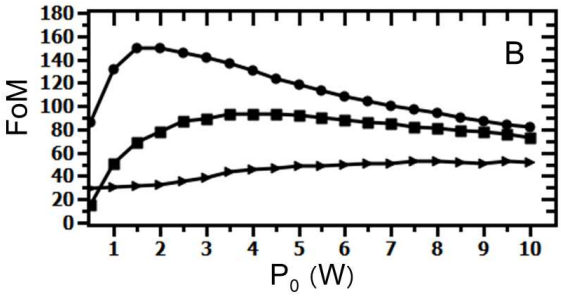

Fig. 8 Figure of merit in fibre B for different values of the initial laser frequency separation LFS : $LFS = 40$ GHz (circles), $LFS = 80$ GHz (rectangles), and $LFS = 160$ GHz (triangles)

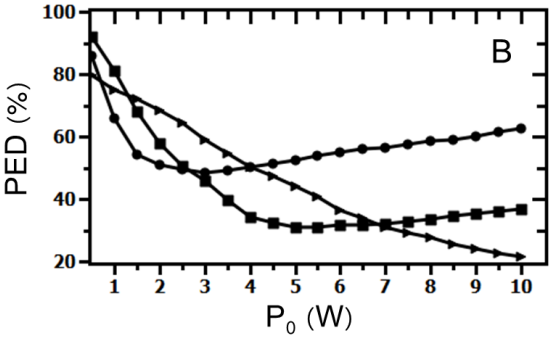

Fig. 9 Pedestal energy content in fibre B in % for different values of the initial laser frequency separation LFS : $LFS = 40$ GHz (circles), $LFS = 80$ GHz (rectangles), and $LFS = 160$ GHz (triangles)

with P_0 again. The minima of PED coincide with the soliton number $N > 1.5$ of the pulses formed in fibre A. More precisely, $N = 1.8$ for $LFS = 40$ GHz and $N = 1.6$ for $LFS = 80$ GHz. Contrary to fundamental solitons with $N = 1$, any solitons with $N > 1.5$ can be regarded as higher-oder solitons [42], the order will grow for higher input powers according to Eq. 7. The increase of the pedestal content with P_0 presented in Fig. 9 goes along with the increase of the soliton order numbers. This result is consistent with results published in Ref. [36]. In the considered input power region, PED decreases continuously for $LFS = 160$ GHz reaching a value of only $PED = 22\%$ for $P_0 = 10$ W. The increase of PED will occur for $P_0 > 10$ W.

A comparison of Fig. 8 and Fig. 9 shows that the increase of FoM for low input powers coincides with the decrease of PED meaning that the most pulse energy gets effectively converted into the pulse peak power via the pulse compression. The increase of PED causes the decrease of FoM for higher values of P_0.

4.2 Figure of merit and pedestal content of fibre B depending on the group-velocity dispersion of fibre A

Fig. 10 shows that the maximum value of FoM of fibre B does not depend on the GVD parameter chosen for fibre A. It shifts, however, to higher values of P_0 as the absolute value of β_2^A increases ($FoM = 93$ at $P_0 = 2$ W for $\beta_2^A = -7.5$ ps^2/km and $FoM = 93$ at $P_0 = 4$ W for $\beta_2^A = -15$ ps^2/km). The decrease of FoM after reaching a maximum is almost equally fast for $\beta_2^A = -7.5$ ps^2/km $\beta_2^A = -15$ ps^2/km. A similar behaviour will also occur for $\beta_2^A = -30$ ps^2/km and higher values of P_0.

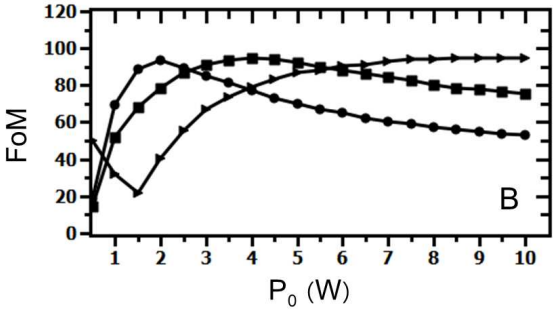

Fig. 10 Figure of merit in fibre B for for different values of the GVD parameter of fibre A: $\beta_2^A = -7.5$ ps^2/km (circles), $\beta_2^A = -15$ ps^2/km (rectangles), and $\beta_2^A = -30$ ps^2/km (triangles))

Fig. 11 shows that, again, the decrease of FoM coincides with a build-up of the pedestal: after a minimum of only $PED = 33\%$ for $\beta_2^A = -7.5$ ps^2/km at $P_0 = 3.5$ W $PED = 30\%$ for $\beta_2^A = -15$ ps^2/km at $P_0 = 5$ W, both curves start increasing. Thus, we have $PED = 56.5\%$ for $\beta_2^A = -7.5$ ps^2/km and $PED = 38\%$ for $\beta_2^A = -15$ ps^2/km at $P_0 = 10$ W. The $PED-$minima coincide with soliton order of $N = 1.9$ for $\beta_2^A = -7.5$ ps^2/km and $N = 1.6$ for $\beta_2^A = -15$ ps^2/km. Again, the soliton order evolution causes the build-up of the pedestal. For $\beta_2^A = -30$ ps^2/km, the $PED-$curve decreases continuously as P_0 increases within the input power range we consider here, $PED = 34\%$ at $P_0 = 10$ W.

Comparing the results obtained in Sec. 4.1 and Sec. 4.2, we see that the optimum system performance is obtained for $\beta_2^A = -15$ ps^2/km and $LFS = 80$ GHz.

5 Intensity noise in Fibre A, B, and C

The intensity noise (IN) coming from fibres A and B, can be strongly detrimental when the pulses propagate through fibre C. The high nonlinearity of this fibre increases the amount of the amplified noise of fibre B which leads to the reduction of the optical signal-to-noise ratio (OSRN) in the frequency domain. In this section, we

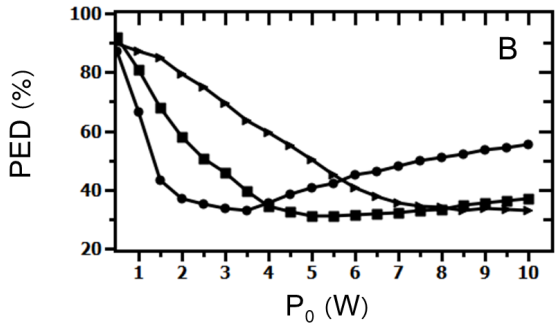

Fig. 11 Pedestal energy content in fibre B in % for for different values of the GVD parameter of fibre A: $\beta_2^A = -7.5$ ps^2/km (circles), $\beta_2^A = -15$ ps^2/km (rectangles), and $\beta_2^A = -30$ ps^2/km (triangles)

investigate IN in fibre B that comes from the amplification of any noise contributed from fibre A. In fibre A, the increase of intensity noise can be caused by modulational instability [41].

The following questions are addressed here:

- How does the level of intensity noise in the amplifying fibre B, i.e. IN^B, depends on the initial LFS and the value of the GVD of fibre A?
- What importance has the initial $IN-$level for all three fibre stages?
- How effective is the filtering technique consisting of two optical bandpass filters we proposed for the experiment?

We define the intensity noise IN as the difference between the maximum peak power within a pulse train at the end of each fibre, i.e. $\max(|\hat{A}|^2)$, and the according peak-power average, i.e. $\langle|\hat{A}|^2\rangle$, in percentage terms:

$$IN = \frac{|\max(|\hat{A}|^2) - \langle|\hat{A}|^2\rangle|}{\langle|\hat{A}|^2\rangle} \cdot 100\%. \qquad (12)$$

Here, we consider three cases of the initial $IN-$power (Eq. 6): the ideal case of $n_0 = 2P_0 10^{-10}$ that conicides with 90 dB OSRN, $n_0 = 2P_0 10^{-8}$ that corresponds to 70 dB OSRN, and $n_0 = 2P_0 10^{-6}$ that corresponds to 50 dB OSRN. The first case is hardly realisable in a real experiment, while two latter ones are, on the contrary, realistic. We use optimised lengths of fibre A and B.

5.1 Noise level in the amplifying stage depending on the initial laser frequency separation

To study of the intensity noise evolution in fibre B as a function of the initial LFS, we chose the following values: $LFS = 40$ GHz, $LFS = 80$ GHz, $LFS = 160$ GHz. The initial intensity noise contribution is generated as a randomly distributed noise floor with the maximal power of $n_0 = 2P_0 10^{-8}$. The GVD parameter of fibre A is $\beta_2^A = -15$ ps^2/km.

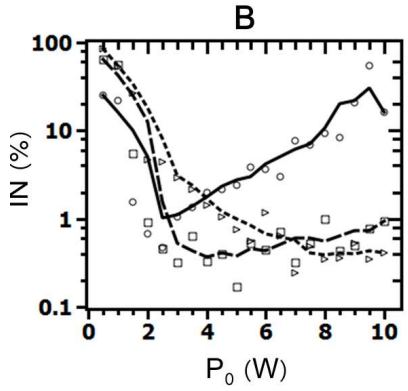

Fig. 12 Intensity noise in fibre B, IN^B, in % vs. input power P_0 in W for different values of the initial laser frequency separation LFS : $LFS = 40$ GHz (circles), $LFS = 80$ GHz (rectangles), and $LFS = 160$ GHz (triangles)

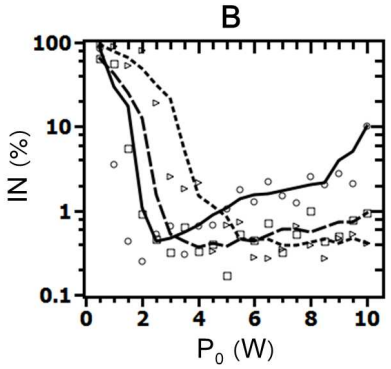

Fig. 13 Intensity noise in fibre B, IN^B, in % vs. input power P_0 in W for different values of the group-velocity dispersion of fibre A β_2^A : $\beta_2^A = -7.5$ ps^2/km (circles), $\beta_2^A = -15$ ps^2/km (rectangles), and $\beta_2^A = -30$ ps^2/km (triangles)

Fig. 12 shows that, for input powers for which fibre A has plateaus in its optimum lengths, the IN^B-level is very high (cf. Fig. 6). In this P_0-region, the optical pulses are not moulded into solitons yet when they propagate through fibre A (cf. Sec. 3). Therefore, they lack the stability and robustness of real solitons to sustain the perturbation that is caused by the parameter change (GVD and nonlinearity) as they enter fibre B. As a result, the pulses break-up which yields a high level of IN in fibre B.

The resemblance of an optical pulse with a real soliton means its stability grow as the value of P_0 approaches the edge of the plateau region. So, the level of IN^B decreases until it reaches a minimum at the plateau edge. Beyond the plateau region, the pulses are robust against the perturbation caused by the fibre parameter change since they are compressed to real solitons in fibre A. This has low intensity noise as a result: $IN < 1\%$ for $LFS = 80$ GHz and $LFS = 160$ GHz. In Sec. 3.1, we showed that the soliton order is higher for smaller LFS. Higher-order solitons are subjected to a break-up which leads to to the increase of intensity noise. This is why IN increases up to ca. 10% for $LFS = 40$ GHz. An optimal system performance is shown for $LSF = 80$ GHz.

5.2 Noise level in the amplyfying stage depenging on the group-velocity dispersion of fibre A

Having the maximal initial noise power of $n_0 = 2P_0 10^{-8}$ generated as a floor and initial laser frequency separation of $LSF = 80$ GHz, we now vary the GDV parameter of fibre A and choose the following values: $\beta_2^A = -7.5$ ps^2/km, $\beta_2^A = -15$ ps^2/km, $\beta_2^A = -30$ ps^2/km.

Fig. 13 shows that for input powers in the plateau region, the value of IN^B is very high. Again, it occurs due to the instability and the resulting break-up of the optical pulses. For higher values of P_0, however, IN^B remains below 1% for $\beta_2^A = -15$ ps^2/km and $\beta_2^A = -30$ ps^2/km and increases up to 10% for $\beta_2^A = -7.5$ ps^2/km.

As discussed in Sec. 3, the soliton order grows as the absolute value of GVD of fibre A decreases. Higher-order solitons incline to the break-up for higher numbers of their order which has an increase of the intensity noise as a result. This is why we observe an increase of IN^B up to 10% for $\beta_2^A = -7.5$ ps^2/km.

The best performance is shown for $\beta_2^A = -15$ ps^2/km, thus, we will use this value for further studies.

5.3 Intensity noise depending on the initial noise level. Effectiveness of the proposed filtering technique

For the study on the intensity noise of all fibre stages, i.e. IN^A, IN^B, and IN^C, we consider three cases of the initial $IN-$power generated as a randomly distributed floor (Eq. 6): $n_0 = 2P_0 10^{-10}$, $n_0 = 2P_0 10^{-8}$ and $n_0 = 2P_0 10^{-6}$. The value of the frequency separation is chosen to be $LFS = 80$ GHz and the GVD parameter of fibre A is set to $\beta_2^A = -15$ ps^2/km.

Fig. 14 shows that the whole system is sensitive to the value of the initial noise power. This dependence begins already in fibre A. Thus, IN^A takes the following values: ca. 0.1% for the ideal case of $n_0 = 2P_0 10^{-10}$, ca. 1% for $n_0 = 2P_0 10^{-8}$, and ca. 10% for $n_0 = 2P_0 10^{-6}$.

In the fibre-A plateau region, the pulses not being real solitons yet and propagating through fibre B are extremely noisy for any values of n_0 due to their instability and the inclination to a break-up. Although one would expect the intensity noise level to increase in the amplifying fibre B, it actually gets slightly suppressed for 2.5 W $\leq P_0 <$ 8 W. Apparently, fibre B has a stabilising effect on the optical pulses in this input power region. For higher values of P_0, fibre B is not adding any addition noise, either.

The nonlinearity of fibre C, however, adds a significant amount of IN to the system, especially if the initial

condition is highly noisy. So, we have IN^C of $< 1\%$ for $n_0 = 2P_0 10^{-10}$, ca. 6% for $n_0 = 2P_0 10^{-8}$, and ca. 40% for $n_0 = 2P_0 10^{-6}$ for the values of P_0-region beyond the plateau region of fibre A. Thus, to keept the level of the intensity noise as low as possible it is advisable to choose a low-noise initial condition.

Now we analyse the effectiveness of the proposed filtering technique. Two 20 dB−filters with 30 GHz bandwidth was suggested to filter the noise coming from the amplifiers (AMP1 and AMP2 in Fig. 1). The filters are modelled by two Gauss functions as described in Sec. 2.2. In our studies, the Gaussians filter the initial noise floor with $n_0 = 2P_0 10^{-6}$ down to $n_0 = 2P_0 10^{-8}$ (cf. Fig. 3). The according results are presented in Fig. 14 as crosses. As one can see, the crosses lie close to the curves that present the $IN-$level for the situation when a noise floor with $n_0 = 2P_0 10^{-8}$ is chosen as initial condition. To be precise, the IN^A_{filter} is ca. 2%, $IN^B_{\text{filter}} < 1\%$, and IN^C_{filter} is less than 12% for $P_0 > 2.5$ W. That means that the proposed filtering technique is highly effective in the suppression of intensity noise and should be deployed in a real experiment.

Fibre A			
P_0, $[W]$	IN	T_c, [ps]	T_p, [ps]
2.0	floor	6.16	1.58
	filtered	6.39	
5.5	floor	6.14	0.67
	filtered	6.28	
9.0	floor	6.15	0.46
	filtered	6.41	

Table 1 Coherence time T_c and FWHM of optical pulses T_p in fibre A for a floor and filtered initial noise with $n_0 = 2P_0 10^{-8}$

Fibre B			
P_0, $[W]$	IN	T_c, [ps]	T_p, [ps]
2.0	floor	1.56	0.06
	filtered	1.61	
5.5	floor	0.66	0.08
	filtered	0.67	
9.0	floor	0.46	0.09
	filtered	0.47	

Table 2 Coherence time T_c and FWHM of optical pulses T_p in fibre B for a floor and filtered initial noise with $n_0 = 2P_0 10^{-8}$

6 Coherence in Fibre A, B, and C

The timing jitter of the optical pulses causes the broadening of the OFC lines. We study the impact of the timing jitter by means of the pulse coherence time T_c that we define as the FWHM of the pulses that arise by a pairwise overlapping of pulse trains generated at two different times, i and $i+1$, and having, accordingly, different randomly generated initial $IN-$level. The overlap function is given by

$$\tilde{g}(t) = \left\langle \frac{A_i^*(t) A_{i+1}(t)}{\sqrt{|A_i(t)|^2_{\max} |A_{i+1}(t)|^2_{\max}}} \right\rangle \qquad (13)$$

where

$$|A_i|^2_{max} = \max(|A_i|^2) \qquad (14)$$

is the maximum norm (cf. [38]). For the calculation of $\tilde{g}(t)$, we use 10 different pulse trains, i. e. $i \in (1, ..., 10)$. A high level of pulse coherence corresponding to low timing jitter is presented when $T_c > T_p$. Note, T_p is the pulse FWHM.

We consider the coherence time T_c for three different values of the input power P_0 and initial noise IN with $n_0 = 2P_0 10^{-8}$ generated as a randomly distributed floor. Afterwards, these results will be compared with the case when the initial noise level with $n_0 = 2P_0 10^{-6}$ is filtered down to $n_0 = 2P_0 10^{-8}$ by means of Gaussian filters as described above. The initial frequency separation is chosen to be $LFS = 80$ GHz.

As one notes from Tab. 1, the pulse width T_p decreases with the input power P_0 in fibre A due to the power-dependent compression process. Thus, we have $T_p = 1.58$ ps for $P_0 = 2.0$ W and $T_p = 0.46$ ps for $P_0 = 9.0$ W. However, for any values of P_0, the coherence time T_c remains almost the same, it slightly varies around the average value of $\langle T_c \rangle = 6.15$ ps that is close to the natural pulse width of $T_0 = 6.4$ ps in fibre A indicating high level of pulse coherence and very low timing jitter.

In fibre B (Tab. 2), the pulse widths T_p slightly increase with the input power P_0. This is the result of the decreasing compression effectiveness for the increasing input powers which we found out in further studies lying beyond the scope of this paper. So, we have $T_c = 0.06$ ps for $P_0 = 2.0$ W, $T_c = 0.08$ ps for $P_0 = 5.5$ W, and $T_c = 0.09$ ps for $P_0 = 9.0$ W. Contrary to fibre A, the value of T_c strongly depends on the initial power: $T_c = 1.56$ ps for $P_0 = 2.0$ W, $T_c = 0.66$ ps for $P_0 = 5.5$ W, and finally $T_c = 0.46$ ps for $P_0 = 9.0$ W. This occurs due to the fact that the pulse pedestal gets destroyed to a large extend as the input power increases. Nonetheless, the coherence T_c is more than 5 times larger than the pulse width T_p meaning still a good coherence performance with low timing jitter.

The optical pulses do not get compressed any further in fibre C (see Tab. 3). However, the values of the coherence time T_c drop after the pulses propagated through fibre C and are only a bit higher than the pulse widths T_p: $T_c = 0.07$ ps for $P_0 = 2.0$ W, $T_c = 0.08$ ps for $P_0 = 5.5$ W, and $T_c = 0.09$ ps for $P_0 = 9.0$ W. The reason for low coherence time is the break-up of the pulse pedestal into pulses with irregular intensity and repetition due to the high fibre nonlinearity.

For the performed studies, the coherence time T_c of the filtered signal lies slightly below the T_c-values of

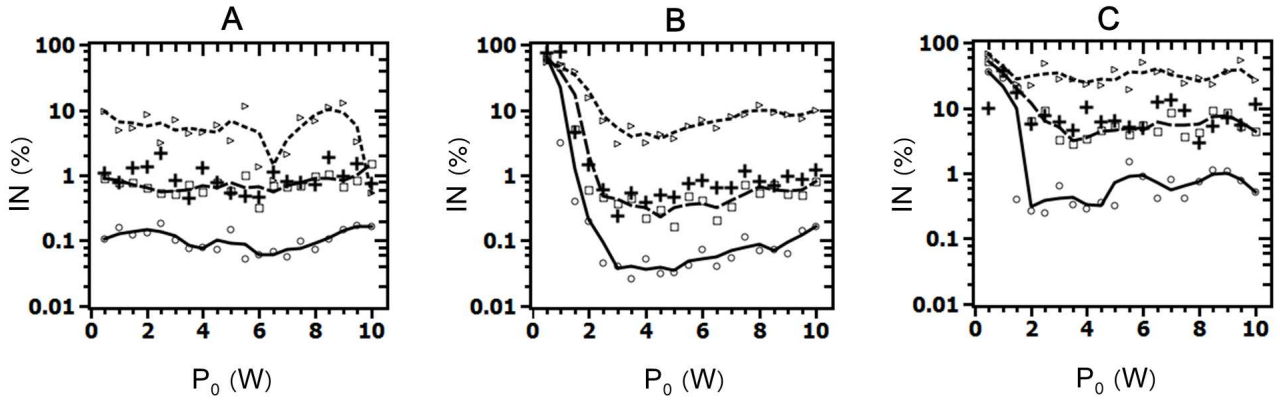

Fig. 14 Intensity noise of fibres A, B, and C, IN^A, IN^B, and IN^C, in % vs. input power P_0 in W for different values of the initial noise power: $n_0 = 2P_0 10^{-10}$ (solid line), $n_0 = 2P_0 10^{-8}$ (dashed line), and $n_0 = 2P_0 10^{-6}$ (dotted line). The crosses present the intensity noise of the filtered signal.

Fibre C			
P_0, [W]	IN	T_c, [ps]	T_p, [ps]
2.0	floor	0.07	0.06
	filtered	0.08	
5.5	floor	0.08	0.08
	filtered	0.09	
9.0	floor	0.09	0.09
	filtered	0.10	

Table 3 Coherence time T_c and FWHM of optical pulses T_p in fibre C for a floor and filtered initial noise with $n_0 = 2P_0 10^{-8}$

the unfiltered (floor) noise. This has only a negligible reduction of the coherent bandwidths. Thus, the proposed filtering technique proved to be effective once again.

7 Experimental data

Using the results from the numerical section where optimum fibre lengths, dispersion values, and input powers were found, we have setup an experimental arrangement to generate frequency combs for calibration of astronomical spectrographs. Fig. 1 shows the schematic of the experimental setup.

In the setup we used (cf. Fig. 1), the EOM carves the initial wave that arises after the combination of both CW lasers into pulse trains with total extension of 20 ns. The first amplifier AMP1 provides an average power of 12 mW. The second amplifier AMP2 raises the average power to a value of 100 mW. The first filter F1 has a bandwidth of 100 GHz, the bandwidth of the second filter F2 is 30 GHz. As the first stage (A) a conventional single-mode fibre with total length of $L^A = 350$ m and the parameters $\beta_2^A = -21$ ps^2/km, $\gamma^A = 2$ W^{-1}km^{-1} was deployed. Instead of an Er-doped fibre (B), a double-clad Er/Yb-fibre with length of $L^B = 17$ m was used. This fibre got pumped with power of 3 W at 940 nm. The fibre parameters are $\beta_2^B = -15$ ps^2/km, $\gamma^B = 2.5$ W^{-1}km^{-1}. Fibre C has the length of $L^C = 3.5$ m and the parameters $\beta_2^C = -0.5$ ps^2/km, $\gamma^B = 10$ W^{-1}km^{-1} at 1550 nm. The initial laser frequency separation was $LFS = 200$ GHz (1.56 nm at 1531 nm) which corresponded to the pulse repetition rate of 200 GHz in the time domain.

Fig. 15 shows typical spectra after fibre A, B, and C, respectively. The spectrum of fibre A ranges from 1546.2 nm to 1560.5 nm, while the spectral bandwidth for fibre B is greatly extended from 1465 nm to 1645 nm. The line intensities in fibre A and B differ, however, in a few orders of magnitude. After propagation through fibre C, it is further broadened to the range between 1400 nm and 1700 nm and the line intensities are better equalised. Characterisation beyond 1700 nm was not possible due to limitations of the spectrometer used in the experiment.

To prove the effectiveness of the proposed system, we use a MUSE-type spectrograph (Fig. 16.1). This spectrograph combines a broadband optical spectrograph with a new generation of multi-object deployable fibre bundles. It is a modified version of the Multi-Unit Spectroscopic Explorer (MUSE): instead of using image slicing mirrors, a 20×20 fiber-fed input is used (Fig. 16.2 and Fig. 16.3). The MUSE instrument itself operates in the wavelength range between 465 nm to 930 nm with a 4096×4096 CCD detector having 15 μm pixels. Its wavelength calibration is performed using the spectral lines from Ne and Hg lamps. The modified MUSE-type spectrograph we used exhibits the same features.

Thus, for the comb to be detectable by a MUSE-type spectrograph, we need to frequency-double the OFC obtained after fibre B into the visible spectral band. For that, an OFC centred at 1560 nm and spanning over 350 nm is focused into a BBO crystal with a thickness of 2 mm by means of a collimator and a focusing objective.

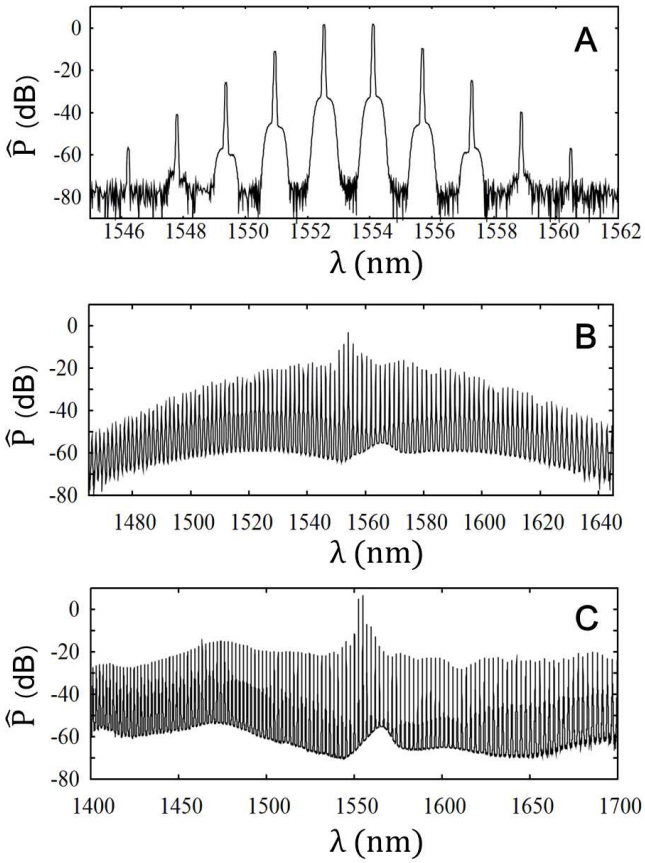

Fig. 15 OFCs obtained after propagation through fibre stages A, B, and C with $LFS = 200$ GHz

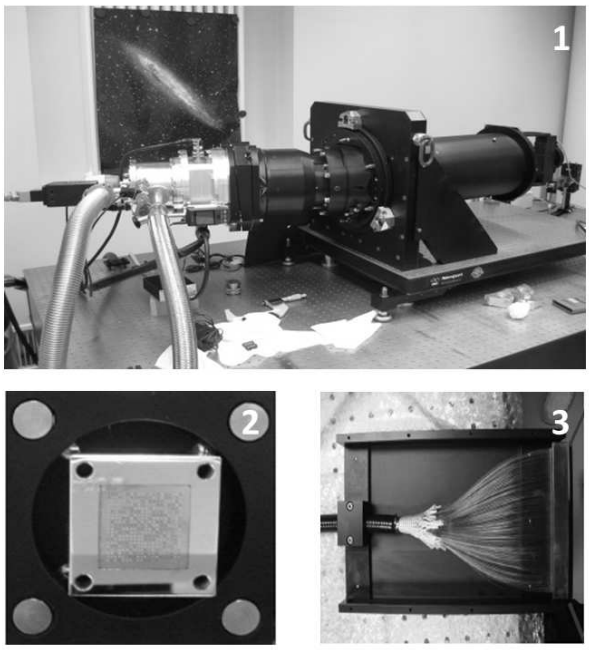

Fig. 16 The MUSE-type spectrograph (1), the input (1) and the output (2) of the fibre bundle

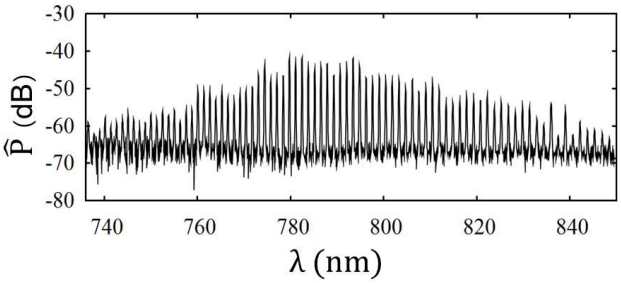

Fig. 17 OFC obtained by means of the frequency-doubling of the output of fibre B

Fig. 17 shows the frequency-doubled spectrum obtained with $LFS = 708$ GHz (5.54 nm at 1531 nm). The spectrum extends from 736 nm to 850 nm and exhibits ca. 80 narrow equidistantly positioned lines. The lines have, however, different intensities which is caused by the frequency-doubling process. The frequency-doubling, however, has not imply a noticeable change of the coherence characteristics of the OFC. The best performance is in terms of the equality of line intensities is achievend in the spectral range between 780 nm and 800 nm.

A comparison between the calibration spectra of a Ne lamp and the frequency-doubled OFC was done using the MUSE-type spectrograph. The time exposure for both, the Ne and comb light, was 30 s, while different exposures were taken with a few minutes of difference between them. Fig. 18 and Fig. 19 show the CCD images for two contiguous spectral regions (each one with 19.5 nm width) covering the range of $780-820$ nm. Each comb line was sampled by 5 pixels. While the comb spectra exhibit bright and uniformly spaced peaks, the Ne light shows only three lines in the spectral region 1 and none in the other region.

In Sec. 3, we drew our attention to the optimisation of the lengths of fibre A and B with the aim to achieve well-compressed optical pulses exhibiting minimal intensity noise. The lengths af stages A and B used for the experiment are close to the lengths obtained via numerial simulations. Thus, a good $IN-$performance was expected. However, the optical amplifiers add a large amount of IN to the OCF. Nevertheless, the comb shows a good OSRN of more than 20 dB with the amount of optical power entering the spectrograph that is well above the detector's noise floor.

To determine the line spacing between the comb lines, the detected light was reduced using a p3d software. Each line was independently fitted using a Gaussian function in order to have an accurate determination of the central wavelength and the line width. Fig. 20 shows the plot of the centre frequency as a function of the comb line.

This was performed for all comb lines and for a representative number of the 400 fibres distributed over the field of view of the spectrograph. The results are summarised in Tab. 7 for several fibres in the fibre bundle. As

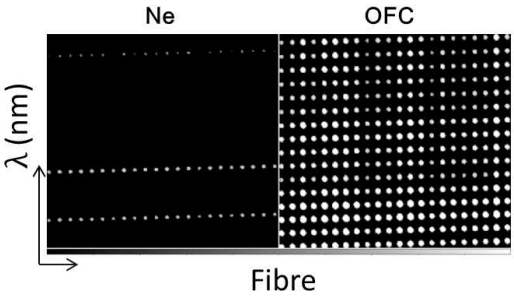

Fig. 18 Comparison between calibration with a Ne lamp and an OFC in spectral region 1 of the MUSE-type spectrograph

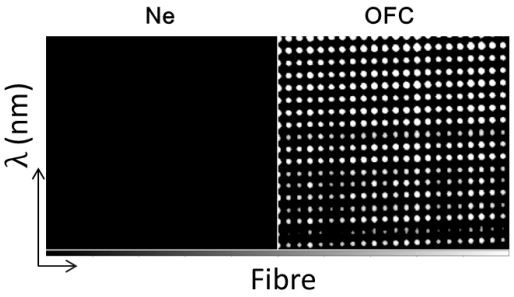

Fig. 19 Comparison between calibration with a Ne lamp and an OFC in spectral region 2 of the MUSE-type spectrograph

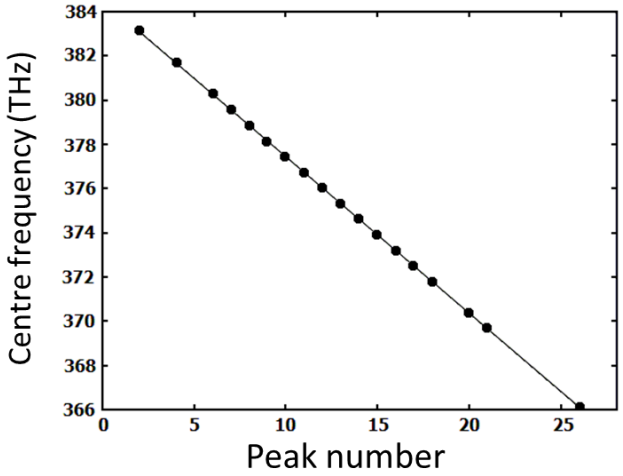

Fig. 20 OFC line spacing for fibre no. 50 of the fibre bundle

one can see, the line spacing changes from 708.5 GHz to 708.8 GHz among the different fibres while the standard deviation for a single fibre is always 0.1 GHz. The main source of this deviation are the errors that arise during the fitting process with the help of Gaussian functions. Combs with this value of standard deviation are acceptable for astronomical application in the low- and medium resolution range.

Fibre no.	Line spacing, [GHz]	Stand. dev., [GHz]
25	708.6	0.1
45	708.7	0.1
50	708.5	0.1
51	708.5	0.1
55	708.5	0.1
100	708.7	0.1
150	708.8	0.1

Table 4 OFC line spacing for different fibres in the fibre bundle

8 Conclusion

We investigated a fibre-based approach for generation of optical frequency combs via four-wave mixing in fibres starting from two CW lasers. This approach deploys an amplifying erbium-doped fibre stage. We performed numerical studies on the fibre length optimisation for different values of the input power P_0 (0.5 W $\leq P_0 \leq$ 10 W), laser frequency separation LSF, $LSF =$ 40 GHz (312.7 pm), 80 GHz (625.5 pm), and 160 GHz (1.25 nm at 1531 nm), and the group-velocity dispersion parameter of the first fibre stage ($\beta_2^A = -7.5$ ps^2/km, -15 ps^2/km, -30 ps^2/km). Depending on the system parameters, the following fibre lengths were achieved via simulations: $150 - 1100$ m for the first fibre stage and $7 - 37.5$ m for the second (amplifying) stage. Since the simulations were performed neglecting the optical fibre losses, the real optimum length of the first fibre stage might be up to 50 m longer, for the second stage up to 10 m.

The pulse compression in the amplifying fibre stage in our approach corresponds to the well-known higher-order soliton compression in dispersion-decreasing fibres. Using optimised fibre lengths, we showed that the undesired pulse pedestal content can be minimised to 30% within the frame of our approach. Having introduced a figure of merit that describes the conversion of the pulse energy into the pulse peak power, we showed that the maximum of the figure of merit does not depend on the group-velocity dispersion parameter of the first fibre stage, but it is inversely proportional to the initial laser frequency separation. Accordingly, to achieve broad comb spectra, one should choose smaller laser frequency separation.

However, we also showed that smaller laser frequency separation leads to the higher intensity noise in the amplifying stage. Our simulations showed that the intensity noise increases up to 10% for the smallest value of the laser frequency separation chosen, i.e. for 40 GHz. For 80 GHz and 160 GHz, it can be kept below 1%. That means to achieve the best possible results, one needs to balance between the figure of merit and the noise performance. In our case, the optimum parameters were $LFS = 80$ GHz and $\beta_2^A = -15$ ps^2/km.

Having chosen the optimum values, we studied the evolution of the intensity noise in all three fibre stages as

a function of the initial intensity noise level. We showed that for the initial noise level that corresponds to 70 dB optical signal-to-noise ratio, the intensity noise in the first fibre is ca. 1% for any values of the input power, is $< 1\%$ in the amplifying fibre, and $< 10\%$ in the third highly nonlinear fibre stage for input powers > 3 W. Moreover, we showed that the optical pulses exhibit high level of coherence in the first and second fibre stage and an acceptable level in the third one.

We also showed that the proposed filtering technique that consists of two 20 dB-filters with 30 GHz bandwidth is highly effective for the controlling of the intensity noise and the coherence properties of the system.

Having used the numerical results, we generated a frequency comb to be used in an astronomical application. For that, we generated a frequency comb with laser frequency separation of 200 GHz (1.56 nm at 1531 nm) in all three fibre stages. To prove the equidistance of the comb lines, we deployed a MUSE-type spectrograph. For that, we frequency-doubled the comb (with frequency separation of 708 GHz) (5.54 nm at 1531 nm) achieved after the second fibre into the visible spactral range. The comb that was detected by the MUSE-type spectrograph ranged between 780 nm and 820 nm. Having plotted the centroids of the comb lines, we realised that the standard deviation of the comb line spacing amounts to only 0.1 GHz (0.8 pm). In the course of further studies, we expect to generate a comb with a bandwidth of 150 nm at 800 nm.

To conclude, the approach we presented here is suitable for astronomical application in the low- and medium-resolution range in terms of noise and stability performance. A possible application taking advantage of our approach can be the 4MOST instrument addressing the research on the chemo-dynamical structure of the Milky Way, the cosmology with x-ray clusters of galaxies, and the Dark Energy [53].

References

1. S. T. Cundiff, J. Yen, Reviews of Modern Physics **75** (2003)
2. J. M. Dudley, G. Genty, F. Dias, B. Kibler, N. Akhmediev, Optics Express **Vol. 17, Issue 24** (2009)
3. G. Yang, L. Li, S. Jia, D. Michaleche, Romanian Reports in Physics **Vol. 65, No. 3** (2013)
4. S. Pitois, J. Fatome, G. Millot, Optics Letters **Vol. 27, No. 19** (2002)
5. C. Finot, J. Fatome, S. Pitois, G. Millot, IEEE Photonics Technology Letters **Vol. 19, No. 21**, (2007)
6. C. Fortier, B. Kibler, J. Fatome, C. Finot, S. Pitois, G. Millot, Laser Physics Latters **Vol. 5, No. 11** (2008)
7. J. Fatome, S. Pitois, C. Fortier, B. Kibler, C. Finot, G. Millot, C. Courde, M. Lintz, E. Samain, Transparent Optical Networks, ICTON'09 (2009)
8. I. El Mansouri, J. Fatome, C. Finot, M. Lintz, S. Pitois, IEEE Photonics Technology Letters **Vol. 23, No. 20** (2011)
9. J. Fatome, S. Pitois, C. Fortier, B. Kibler, C. Finot, G. Millot, C. Courde, M. Lintz, E. Samain, Optics Communications **283** (2010)
10. K. E. Webb, M. Erkintalo, Y. Xu, N. G. R. Broderick, J. M. Dudley, G. Genty, S. G. Murdoch, Nuture Communications **5** (2014)
11. K. Griest, J. B. Whitmore, A. M. Wolfe, J. X. Prochaska, J. C. Howk, G. W. Marcy, The Astrophysical Journal **708** (2010) 158-170
12. S. Osterman, S. Diddams, M. Beasley, C. Froning, L. Hollberg, P. MacQueen, V. Mbele, A. Weiner, Proceedings of SPIE **6693** (2007)
13. S. Osterman, G. G. Ycas, S. A. Diddams, F. Quinlan, S. Mahadevan, L. Ramsey, C. F. Bender, R. Terrien, B. Botzer, S. Sigurdsson, S. L. Redman, Proceedings of SPIE **8450** (2012)
14. G. G. Ycas, F. Quinlan, S. A. Diddams, S. Osterman, S. Mahadevan, S. Redman, R. Terrien, L. Ramsey, C. F. Bender, B. Botzer, S. Sigurdsson, Optics Express **Vpl. 20, No. 6** (2012)
15. A. Loeb, The Astrophysical Journal **499** (1998)
16. W. L. Freedman, Proceeding of the National Academy of Sciences USA **95(1)** (1998) 2-7
17. M. T. Murphy, C. R. Locke, P. S. Light, A. N. Luiten, J. S. Lawrence,Monthly Notices of the Royal Astronomical Society **000** (2012)
18. D. F. Phillips, A. G. Glenday, Ch.-H. Li, C. Cramer, G. Furesz, G. Chang, A. J. Benedick, L.-J. Chen, F. X. Kärtner, S. Korzennik, D. Sasselov, A. Szentgyorgyi, R. L. Walsworth, Optics Express **Vol. 20 No. 13** (2012)
19. M. T. Murphy, T. Udem, R. Holzwarth, A. Sizmann, L. Pasquini, C. Araujo-Hauck, H. Dekker, S. D'Odorico, M. Fischer, T. W. Hänsch, A. Manescau, Monthly Notices of the Royal Astronomical Society **Vol. 380, No. 2** (2007)
20. D. A. Braje, M. S. Kirchner, S. Osterman, T. Fortier, A. Diddams, European Physical Journal D **Vol. 48, Issue 1** (2008)
21. T. Wilken, C. Lovis, A. Manescau, T. Steinmetz, L. Pasquini, G. Lo Curto, Proceedings of SPIE **7735** (2010)
22. T. Steinmetz, T. Wilken, A. Araujo-Hauck, R. Holzwarth, T. W. Hänsch, L. Pasquini, A. Manescau, S. D'Odorico, M. T. Murphy, T. Kentischer, W. Schmidtt, T. Udem, Science **Vol. 321, No. 5894** (2008)
23. H.-P. Doerr, T. J. Kentischer, T. Steinmetz, R. A. Probst, M. Franz, R. Holzwarth, T. Udem, T. W. Hänsch, W. Schmidt, Proceedings of SPIE **8450** (2012)
24. G. Lo Curto, A. Manescau, G. Avila, L. Pasquini, T. Wilken, T. Steinmetz, R. Holzwarth, R. Probst, T. Udem, T. W. Hänsch, Proceedings of SPIE **8446** (2012)
25. P. Del'Haye, A. Schliesser, O. Arcizet, T. Wilken, R. Holzwarth, T. J. Kippenberg, Nature **450** (2007)
26. P. Del'Haye, T. Herr, E. Gavartin, M. L. Gorodetsky, R. Holzwarth, T. J. Kippenberg, Physical Review Letters **107** (2011)
27. S. V. Chernikov, E. M. Payne, Applied Physics Letters **63** (1993)
28. Z. Tong, A. O. J. Winberg, E. Myslivets, B. P. P. Kuo, N. Alic, S. Radic, Optics Express **Vol. 20, No. 16** (2012)
29. E. Myslivets, B. P. P. Kuo, N. Alic, S. Radic, Optics Express **Vol. 20, No. 3** (2012)
30. T. Yang, J. Dong, S. Liao, D. Huang, X. Zhang, Optics Express **Vol. 21, Issue 7** (2013)

31. J. M. Chavez Boggio, A. A. Rieznik, M. Zajnulina, M Böhm, D. Bodenmüller, M. Wysmolek, H. Sayinc, J. Neumann, D. Kracht, R. Haynes, M. M. Roth, Proceedings of SPIE **8434** (2012)
32. M. Zajnulina, J. M. Chavez Boggio, A. A. Rieznik, R. Haynes, M. M. Roth, Proceedings of SPIE **8775** (2013)
33. M. Zajnulina, M. Böhm, K. Blow, J. M. Chavez Boggio, A. A. Rieznik, R. Haynes, M. M. Roth, Proceedings of SPIE **9151** (2014)
34. Wen-hua Cao, P. K. A. Wai, Optics Communications **221** (2003)
35. S. V. Chernikov, E. M. Dianov, Optics Letters **Vol. 18, No. 7** (1993)
36. Q. Li, J. N. Kunz, P. K. A. Wai, Journal of Optical Society of America B **Vol. 27, No. 11** (2010)
37. P. Colman, C. Husko, S. Combrie, I. Sagnes, C. W. Wong, A. De Rossi, Nature Photonics **Vol. 4** (2010)
38. G. P. Agrawal, *Nonlinear Fiber Optics* (Academic Press, 2013)
39. S. M. Kobtsev, S. V. Smirnov, Optics Express **Vol. 16, No. 10** (2008)
40. S. M. Kobtsev, S. V. Smirnov, Optics Express **Vol. 14, No. 9** (2006)
41. S. M. Kobtsev, S. V. Smirnov, Optics Express **Vol. 13, No. 18** (2005)
42. J. R. Taylor, *Optical Solitons: Theory and Experiment* (Cambridge University Press, 2008)
43. S. Balac, Fernandez, F. Mahe, F. Mehats, R. Texier-Picard, HAL **00850518v1** (2013)
44. A. Cerqueira S. Jr., J. M. Chavez Boggio, A. A. Rieznik, H. E. Hernandez-Figueroa, H. L. Fragnito, J. C. Knight, Optics Express **Vol. 16, No. 4** (2008)
45. N. F. Smyth, Optics Communications **175** (2000)
46. L. F. Mollenauer, R. H. Stolen, J. P. Gordon, W. J. Tomlinson, Optics Letters **Vol. 8, No. 5** (1983)
47. H. A. Haus, IEEE Spectrum **0018-9235** (1993)
48. A. A. Voronin, A. M. Zheltikov, Physical Review A **Vol. 78, Issue 6** (2008)
49. T. Inoue, S. Namiki, Laser and Photonics Review **2, No. 1** (2008)
50. S. A. S. Melo, A. Cerqueira S. Jr., A. R. do Nascimento Jr., L. H. H. Carvalho, R. Silva, J. C. R. F. Oliveira, Revista Telecomunicacoes **Vol. 15, No. 2** (2013)
51. G. P. Agrawal, *Applications of Nonlinear Fiber Optics* (Academic Press, 2008)
52. F. Mitschke, *Fiber Optics. Physics and Technology* (Springer, Berlin Heidelberg 2009)
53. R. S. de Jong et. al, Proceedings of SPIE **8446** (2012)